Supporting Information

Freudenburg et al. 10.1073/pnas.1311716111

SI Text

Overview of Data Collected. Data were collected from five patients with intractable epilepsy who required invasive monitoring with intracranial electrode arrays for seizure localization (see Table S1 for subject demographics). Between 48 and 64 electrodes were implanted per patient. Multiple runs of the full 36-word task (Fig. S1*A*) were recorded for each subject, resulting in four to six datasets per subject. Eight-eight frequencies (exponentially sampled from 1 to 338) were analyzed for each channel of recorded electrocorticographic (ECoG) data over the entirety of the task recordings. There were six cognitive task comparisons (i.e., rest vs. all spoken words, [i] vs. [ɛ], [i] vs. [æ], [i] vs. [u], [ɛ] vs. [æ], [ɛ] vs. [u], and [æ] vs. [u]) that were analyzed. The rest condition was defined as the period of 0.5–0 s before the audio cue was given. Thirty-seven time slices (Fig. S1*B*) were analyzed for each trial. Between 144 and 216 valid trials were recorded from a given patient. In total, 222 hypotheses were tested per subject, giving an expectation of about five falsely discovered positive tests using the Benjamini-Hochberg procedure (1). A summary of the data characteristics of this study is provided in Table S2.

Rationale for Methodological Approach. When dealing with a very complex dynamic system (i.e., the brain), one can use a simple analysis that may provide complex results or use a complex analysis that provides more simplified results. There is a fundamental tradeoff in either approach. With a more classic signal analysis (e.g., covariance/coherence between two electrodes), the results are straightforward to interpret, but as the number of variables increase (numerous electrodes and numerous frequency bands), the ability to interpret the findings becomes more difficult. Conversely, using more complex analyses, which can identify multidimensional relationships in the data, can be more difficult to interpret from an electrophysiologic/mechanistic standpoint in how these analytic tools actually represent brain function.

It is in this light that we have attempted to strike a balance. Because the power in an electrocorticographic signal drops off at a $1/f$ scale, using a traditional measure of correlation of a raw signal would have limited the assessment of interactions between electrodes to the lower frequencies. This limitation would have essentially excluded assessment of higher gamma rhythms, which contribute minuscule amounts to the total signal in terms of magnitude of power and when present are unlikely to have a consistent phase relationship between electrodes (but are quite physiologically relevant). Also, when cortical activation using field potentials is considered, amplitude modulation has been found to be a very meaningful measure associated with cognitive tasks. Moreover, frequency subbands (e.g., mu, beta, and gamma, gamma subbands) have also been shown to have independent behavior during a cognitive task (2–4). If one were to take a correlation matrix across all these metrics [location and multiple signal characteristics such as event-related potentials (ERPs) or coherence of frequency bands and amplitude modulation], identifying trends would be too complex. Also, because of the very high dimensionality of such a matrix, there will be a high probability for spurious/noisy correlations. This high dimensionality makes it difficult to separate noise from physiologic signal. Thus, integrating across all these dimensions (location, frequency, and signal characteristics) requires some form of data-driven dimensionality reduction [i.e., choosing amplitude modulation and using principal component analysis (PCA) in the frequency and anatomic domain] to allow for statistically meaningful interpretation of the data.

For this aggregated pattern to then be correlated to a cognitive task, we chose a discriminant function analysis (DFA). DFA is a method used to find a weighted pattern of time series variables that maximally discriminate the time series into specified groups. DFA has been shown to give better results than the more popular method of logistic regression when the sample sizes are on the order of 50 or less per condition (5), which was the case for this work. Again, on high-dimensional data, a PCA decomposition gives a low-dimensional representation of the time series data, and it is common to use DFA in this low-dimensional space. The above approach was critical to test our hypothesis that networks would share a multispectral interaction because it necessarily integrated across anatomic locations and across frequencies scales. This hypothesis is also why affinity propagation was subsequently used. This affinity propagation enabled us to cluster the spatio-spectral patterns without a priori assumptions regarding the number of clusters, expected spectral patterns, or assumptions regarding the similarity or dissimilarity of the spatio-spectral patterns. Finally, scaling these network-related findings against known physiologic mechanisms (i.e., single-site amplitude modulation) required the use of a Monte Carlo (MC) P value to enable a valid comparison of two very different physiologic measures. The MC P value has the advantage that the data do not need to give a Gaussian distribution of the test statistic to evaluate the significance of the test condition. In addition, MC P values are comparable across different test statistics for different measurements because the same null hypothesis is tested (6). This property allows for comparison of the MC P values computed for the functional spectral network to those of the amplitude response.

A schematic overview of the analysis performed in this paper is given in Fig. S5. Here we explain the figure and notation used on the basis of key analysis steps (indicated by *A*–*F* in the figure).

For those who wish to have the primary code used in this analysis or the simulated data to test the code and the use of it, please contact Zachary V. Freudenburg at voges78@gmail.com.

Detailed Description of Analysis. To begin, the ECoG signal was composed of temporal samples from each recorded channel. In the figure and this section, the temporal and channel dimensions of the ECoG signal were indexed as t = index through recorded ECoG samples (recorded at 1,200 Hz); and c = index through recorded ECoG channels 1 to C, where C is the number of for a given subject.

The result of the Gabor Wavelet Dictionary analysis was the spatio-spectral signal denoted as $SPs(c, f, t)$, where f was the index through the analyzed frequency bin centers. Frequency bin centers were unique rounded integers based on the exponential distribution of 2 to the power of 0–8.4 in 87 steps of 0.06 (i.e., $\text{unique}(\text{round}(2^{[0:0.06:8.4]}))$).

For the functional spectral network (FSN) analysis, the additional preprocessing step of PCA was performed on the spatial-spectral signal (SPs) over the temporal dimension. The first 100 principal components, based on percent signal variance, and corresponding component scores (i.e., the transformed PCA space values corresponding to each spatial-spectral data point) were denoted, respectively, as $PC_{1:100}(c, f)$ and $PCs_{1:100}(t)$.

The task cue labels and voice onset times (VOTs) were used to define 37 time periods before and after VOT (main text), indexed by τ and seven cognitive subtask comparisons (main text), indexed by l. These time periods and task conditions were then used to define a label vector over trials for each τ and l denoted as $Labels_{\tau,l}(trial)$.

The rest of the analysis was then done using the time periods, and task conditions of the $Labels_{\tau,l}$ signal were then used to analyze the *SPs* and $PCs_{1:100}$ signals. This approach allowed all calculations using the $Labels_{\tau,l}(trial)$ structure to be redone multiple times based on pseudolabels formed from randomly shuffling the trials 1,000 times according to the MC *P* value statistic procedure (6).

The mean percent variance accounted for was 86%. There was a notable difference in the percent variance accounted for between the two subjects who had 64 electrode grids (74% and 75%) and those who had 48 electrode grids (96%, 91%, and 90%). The relatively smaller percent variance accounted for by the first 100 principal components in the 64 electrode subjects indicates that additional electrodes add additional independent spectral features to the data, which is expected.

Selection of the best amplitude response. Standard R^2 analysis is performed on $SPs(c, f, t)$ over trials according to the $Labels_{\tau,l}$ structure to produce $R2_{\tau,l}(c,f)$, which was the signed R^2 value per each channel (c) and frequency (f) at each time period (τ) and cognitive task comparison (l).

The single best amplitude response (AR) per τ and l was defined according to the following procedure: (*i*) loop through each channel (c) and find continuous frequency ranges $F_{c,i}(f_i, f_{i+1}, f_{i+2}, \ldots, f_{x+n})$, such that the sign of $R2_{\tau,l}(c,f_i) = R2_{\tau,l}(c,f_{i+j})$ and the *P* value of $R2_{\tau,l}(c,f_{i+j}) < 0.05$ for all $0 \le j \le n$; (*ii*) choose the frequency range $F_{c,i}$ that maximizes $\sum_{j=0}^{n} R2_{\tau,l}(c,f_{i+j})$ as the best AR; and (*iii*) calculate the AR signal $[ARs_{\tau,l}(trial)]$ for the best frequency range $F_{c,i\ldots k}$ as

$$ARs_{\tau,l}(trial) = \frac{1}{n}\sum_{j=0}^{k} SPs_{\tau}\left(c, f_{i+j,trial}\right).$$

$ARs_{\tau,l}(trial)$ was then used to compute the $ARs_{\tau,l}$ R^2 value.

The *P* value for significance was obtained by converting the coefficient of determination by a generalized Fisher's method, where $F = [r2/(p-1)]/[(1-r2)/(n-p)]$. *F* is the *F*-statistic, *r*2 is the coefficient of determination, *p* is the number of compared processes (active movement/rest), and *n* is the number of observations (number of trials). Once the *F*-statistic is calculated, this was then converted to a *P* value using a table of *F*-statistics.

DFA was used to determine the covarying spatio-spectral patterns that best discriminated the trials for each cognitive task condition pair l and time period τ. The hear-and-repeat task was used to define seven different cognitive tasks as follows: (*i*) all spoken words vs. the preceding "rest," (*ii*) "ee" words vs. "eh" words, (*iii*) "ee" words vs. "ah" words, (*iv*) "ee" words vs. "oo" words, (*v*) "eh" words vs. "ah" words, (*vi*) "eh" words vs. "oo" words, and (*vii*) "ah" words vs. "oo" words. The patterns were defined by solving

$$DF\ Labels_{\tau,l}(trial) = a + b_1 \times PCs_1(trial), \ldots, + b_{100} \times PCs_{100}(trial),$$

using linear regression, where $DF\ \ Labels_{\tau,l}(trial)$ was 1 for each trial from the first task of condition l (where two cognitive subtasks were contrasted with each other; main text) for time period τ and 0 for each trial from the second task condition of l.

We then defined $\hat{b} = b_1, \ldots, b_{100}$ as the discriminant function in the principle component space.

Calculation of discriminant functions patterns in spatio-spectral space. Next we calculated the spatio-spectral pattern for each discriminant function as

$$ssDF_{\tau,l} = \hat{b}_{\tau,l}^{-1} * S^{-1} \times PC_{1:100}^{\sim 1},$$

where $PC_{1:100}^{\sim 1}$ was the pseudo-inverse of the component matrix, and S^{-1} was the inverse of the singular value matrix. $ssDF_{\tau,l}$ was then reshaped to the channel by frequency bin matrix $ssDF_{\tau,l}(c,f)$.

Use of affinity propagation to find clusters of spectrally similar electrodes within each $ssDF_{\tau,l}$. The spatio-spectral disciminant function pattern $ssDF_{\tau,l}(c,f)$ was used as the basis for grouping channels with similar amplitude differences between the cognitive tasks of condition pair l and time period τ using the affinity propagation clustering algorithm (7). In our use of affinity propagation, each channel (c) was a data point with features $ssDF_{\tau,l}(c, f_{1:88})$ over the 88 frequency bins. The similarity ($s_{n,m}$) between data points c_n and c_m was calculated as

$$s_{n,m} = \sum_{i=1}^{88} ssDF_{\tau,l}(c_n, f_i) \times ssDF_{\tau,l}(c_m, f_i).$$

Affinity propagation does not predefine a number of clusters but uses a message passing protocol to converge to a number of clusters. Hence, the number of clusters found was variable for each $ssDF_{\tau,l}$. The number of clusters can be influenced by setting a self-affinity level for each data point (i.e.: channel in this case) that varies how likely it is that each data point becomes its own cluster. It is standard to make this equal for each data point, and we used a value that led to slightly fewer clusters than the standard value recommended in ref. 7. The number of channel clusters varied from two to nine across all $ssDF_{\tau,l}$ for each subject. We used $\{k\}$ to denote the set of all channels in a given cluster.

Calculation of spectral cluster responses. The relevance of a channel cluster $\{k\}$ within a given spatio-spectral discriminant function pattern $ssDF_{\tau,l}$ was computed on the cluster signal given by

$$CLs_{\tau,l,k}(trial) = \sum_{c \in \{k\}} \sum_{j=1}^{88} ssDF_{\tau,l}(c, f_i) \times SPs_{\tau}\left(c, f_j, trial\right).$$

As depicted in Fig. S5, R^2 analysis was performed on $CLs_{\tau,l,k}$ to determine the relevance of each subgroup of spectrally similar channels to the cognitive task discrimination of the total discriminant function $ssDF_{\tau,l}$.

Generally speaking, this equation enables one to identify a correlation measure (R^2) for the discriminant function measures (i.e., spatial-spectral pattern) and amplitude response in an equivalent fashion. This equation takes patterns identified by the discriminant function that are characterized by frequency amplitude changes and electrode location (i.e., the spatial-spectral pattern), and it matches to spatial-spectral patterns in data from one condition to another condition. It is constrained in such a way that it should match one positively and the other negatively. The match between the spatial-spectral patterns of two conditions and the discriminant function was computed in this way so that the difference between conditions reflected in the DFs can be expressed in terms of an *r*2 value. This same method can also be used for amplitude response (i.e., a single site, with a single frequency band) and for FSN (i.e., a subset of electrodes within a discriminant function).

Definition of FSNs. FSNs were defined as the minimal subset of spectral clusters needed to discriminate a cognitive task condition. This minimal subset of channels was defined as follows: (*i*) sort clusters, $CLs_{\tau,l,k}$, by R^2 value in descending order $k_{\max}, \ldots, k_{\min}$; (*ii*) iterate through clusters $i = k_{\max}, \ldots, k_{\min}$ and calculate the R^2 value of $\sum_{j=\max}^{i} CLs_{\tau,l,k_i}$; (*iii*) use MC *P* value statistics to determine at which i the R^2 value of $\sum_{j=\max}^{i} CLs_{\tau,l,k_i}$ becomes significant; and (*iv*) include all channels in the FSN that were in the combined cluster that first reaches significance, such that

$$FSN_{\tau,l} = ssDF_{\tau,l}(c \in \{k_{\max}, \ldots, k_i\}, 1{:}88).$$

Hence, the discriminative value of $FSN_{\tau,l}$ was computed by performing R^2 analysis on the response of each FSN, defined as:

$$FSNs_{\tau,l}(trial) = \sum_{c\in\{k_{\max},\ldots,k_i\}} \sum_{j=1}^{88} ssDF_{\tau,l}(c,f_i) \times SPs_{\tau}(c,f_j,trial),$$

which was found to have a significant MC P value. This MC P value was then directly compared with that of $AR_{\tau,l}$. The MC P value was computed by comparing the R^2 value of $FSN_{\tau,l}$ to a distribution of 1,000 R^2 values gained from pseudo-FSNs with the same numbers of channels as that included in $\{k_{\max},\ldots,k_i\}$. All steps performed using cognitive task labels per trial, indicated by the gray background in Fig. S5, were repeated using randomly shuffled versions of $Labels_{\tau,l}$ to generate the MC distribution of R^2 values for the pseudo-FSNs with equal numbers of included channels.

Analysis Validation with White Noise Data and Simulated Spectral Events Data. The methods used to define FSNs are unique in their application to ECoG spectral data and therefore warrant additional validation on simulated data, in which a ground truth is known. To this end, we replaced the actual ECoG signals (real data) with two forms of known ground truth data.

First, a random white noise signal was created (white noise data) for each subject. Second, a simulated microphone response locked spectral events signal was created (simulated spectral events data).

Both types of simulated data were run through the exact same analysis as the real data. This analysis was done by simply replacing the real ECoG signal with an equal amount of simulated data. Trial timing based on microphone signal and all other subject-specific and non–subject-specific parameters were kept the same. This procedure was done for every dataset from all five subjects. Only the rest vs. rest cognitive task was tested for the validation, and hence only the VOTs and no specific phoneme labels were used for each trial.

In this section, we first discuss the specifics of the two types of simulated data and then present the validation results they produced in Fig. S6.

Creation of white noise and spectral event simulated data. The white noise signal was created by using the standard MATLAB random signal generator that generates random numbers between 0 and 1. An equal number of signal samples as the original real data were generated. The raw signal was replaced before Gabor Wavelet Dictionary spectral analysis and normalization of the spectral response were done, and no scaling factor of the randomly generated numbers was performed to produce the white noise signal.

Creation of the simulated spectral events data was a more complex process. We started with random signals generated in the same way as the white noise data. Then frequency events were added to temporal periods of the signal that were time-locked to VOTs from the real data microphone signal in a subset of 24 electrode channels. The same channels (1–4, 9–12, 17–20, 25–31, and 33–39), which comprised one corner of grid, were chosen for both the 64 electrode and 48 electrode grids.

These frequency events consisted of an alpha range frequency (14 Hz) and a broadband gamma range (65–95 Hz) frequency component being added to the noise signal. The alpha band events were added by first creating a sine wave at 14 Hz and then windowing it with a Hann window that spanned from −0.5 to 0.5 s from VOT. The alpha band events were then scaled using the scaling factor of $R[1/\log(f)]$, with $f = 14$ and R being a random number between 0 and 1, and then added to the period of the signal from 600 samples before (0.5 s) to 600 after VOT for each trial. The gamma band events were created by first creating a white noise signal and then band pass filtering the signal between 65 and 95 Hz. The gamma signal was then scaled by the factor of $1/\log(f)$, with $f = 65$, windowed using a Hann window and added to the simulated signal period that spanned from −0.3 (630 samples) to 0.1 s (120 samples) from VOT for each trial.

Simulated data results. Fig. S6 summarizes the comparison of the results of running the simulated data through the analysis to that of the real data. Throughout the figure, the color scheme of red, gray, and green is used to indicate the results for real data, white noise, and simulated spectral events, respectively. Fig. S6 *A* and *B* summarizes the results of the PCA run on simulated data. Fig. S6*A* plots the mean (solid lines) and SE (shaded areas) over the five subjects of the percent variance in the simulated data accounted for by the first 100 PCs on a log scale. The log scale highlights the differences between the real, white noise, and simulated spectral events in the first several PCs. It can be seen that the percent variance accounted for in the white noise data only changes slightly over the first 100 PCs, indicating that there are no dominant patterns of covariance of spectral features in the data. In contrast, the simulated spectral events data shows two dominant PCs that clearly account for more variance than the white noise. This result is expected because two spectral bands with different temporal spans (causing two spectral patterns) were added to a white noise background. This trend is also present in Fig. S6*C*, which gives spatial-spectral plots (with electrode channel plotted on the x axis and frequency plotted from low at the bottom to high at the top on the y axis) PCs 1, 5, 10, 50, and 100 for the real (top row), white noise (middle row), and simulated spectral events (bottom row) for subject 1. The white noise PCs are seen to remain similar in their lack of spatial-spectral structure (indicated by a lack continuous bands of amplitude change on the y axis and/or channels with similar frequency patterns on the x axis) for all five example PCs. In contrast PC 1 of the simulated spectral events has clear spatial-spectral structure, which is exemplified by the group of 24 channels with increases in amplitude from 65 to 95 Hz. However, PCs 5, 10, 50, and 100 of the simulated spectral events data demonstrate the same lack of spatial-spectral structure as the white noise PCs. The fact that the PC structure of the simulated spectral events data are generally the same as that of the white noise data, with the exception of the first two PCs, is again highlighted by Fig. 5*B*, which plots the distributions over the five subjects of the total percent variance accounted for by the first 100 PCs for the three data types (the boxes from left to right for real, white noise, and simulated spectral event data, respectively). The figure shows that, despite the first 2 PCs, the first 100 PCs of simulated spectral events data does not account for significantly more variance than those of the white noise data. This result demonstrates that the patterns of amplitude covariance added to the simulated spectral events data account for a small portion of the spectral features of the data.

Taken together, the PCA plots also highlight two characteristics of the real data. First, the real data have spectral patterns that are diverse but are well accounted for by 100 PCs. It can also been seen that the real data have dominant PCs, similar to the first two PCs of the simulated spectral events data. However, the percent variance remains above the white noise level until around PC 50, indicating a much more diverse set of independent spectral patterns in the real data. This increased diversity is also demonstrated by the fact that the real data PCs show marked spatial-spectral structure at PCs 1, 5, 10, and 50, whereas PC 100 of the real data shows some spatial-spectral structure but looks most similar to white noise PCs. In addition, the total percent variance accounted for by the first 100 PCs of the real data are significantly higher than both the white noise and simulated spectral events data. Second, there are both uniform noise and electrophysiological spatial-spectral structure in the real data. The real data PCs also demonstrate that the first PCs (which account for the most variance) have a spatial-spectral structure of frequency-specific amplitude changes that are global (across all electrodes) in nature and not anatomically focal. This type of spatial-spectral structure is likely due to uniform (in contrast to white noise) components of the real signal. The spatial-spectral pattern of PC 50

demonstrates a spatial-spectral structure with anatomically local and spectrally broad features, which is more similar to that expected from electrophysiological components of ECoG data. The spatial-spectral structure of PCs 5 and 10 demonstrate both uniform noise and electrophysiological components.

The second feature of the methods highlighted by the validation results is that the DFs are able to successfully combine the PCs to isolate spatial-spectral structure that is correlated to the cognitive task. Fig. S6*D* shows that the spatial-spectral patterns of the DFs for the simulated spectral events data (bottom row) reflect those that are expected by the spectral events that were added to the signal, whereas those of the white noise (middle row) are very similar to the spatial-spectral patterns of PCs for white noise. It should also be noted that even nonsignificant time periods, such as time periods 1 and 1.5 s (bottom left two plots), show the spatial-spectral structure of the added theta band spectral events. This result is due to the fact that these event shift the mean of the theta band and cause the time point outside to the added events to have a negative amplitude in the normalized data. Fig. S6*D* summarizes the number of significant temporal periods (rejected null hypotheses among the 37 time periods tested) found by the analysis (using an MC *P* value cutoff of 0.05) for the three types of data. Each data type for which the number of significant hypothesis was significantly greater (using a pairwise *t* test over subjects) than the number of expected false discoveries is indicated with an asterisk. The number of false discoveries was calculated using the Benjamini–Hochberg procedure that takes into account the distribution of the *P* values (in our case MC *P* values) computed for each tested hypothesis. The plot shows that the numbers of significant time points in the simulated spectral events data are less than that of the real data. This result is to be expected given the time span of the simulated spectral events. However, the numbers were significantly higher than the number of expected false discoveries (mean of 4.6), whereas the number for white noise data was not.

Fig. S6 *F*–*H* gives examples of star plots for the FSNs computed from the DFs for the three data types. Although some DFs were found for the white noise data, the blank plot in Fig. S6*G* highlights that these did not achieve statistical significance found by the FSN method. Fig. S6*H* shows that the FSN for a significant time period, such as that centered around 0 s, is spatially constrained to the electrode channels to which the simulated spectral events were added (i.e., channels 1–4, 9–12, 17–20, 25–31, and 33–39).

Impact of Epilepsy on Physiologic Data. The use of invasively monitored human subjects is both a strength and a weakness of the study. Specifically, this clinical scenario provides unique access to human cortical electrophysiology that is distinct from noninvasive recording and imaging modalities, as well as from animal models. These patients, however, by definition have a pathologic condition affecting their brain that requires placement of intracranial electrodes. Previous work has demonstrated that global synchronization increases substantially during a seizure and globally decreases before a seizure in the context of mesial temporal lobe epilepsy (8). Also, in the context of generalized epilepsy (absence seizures in which no seizure focus is present), there is a complex interplay between long-range desynchronization and local synchrony (9).

With these very relevant considerations, several features in this study support a more generalized phenomenon beyond the pathophysiology associated with epilepsy.

First, this study fundamentally hinges on the performance of a cognitive speech task in patients with a focal seizure onset zone that did not involve speech cortex. Their seizure onset zone was determined by ongoing monitoring, and their speech areas were defined by stimulation mapping (Fig. S7). All of the patients had normal speech function as assessed by a neuropsychologist. In addition, the speech paradigm was performed on a day when no seizures were recorded. Finally, the study was designed to identify very specific elements of a cognitive task (phonemes), which would be unlikely to be accounted for by random pathologic events (ictal or interictal discharges). Thus, taken together, the pathologic cortex was anatomically separate and did not affect baseline speech function, and more generalized effects (i.e., the seizure) were temporally distinct from the time the experimental task was performed.

Second, given these precautions, the impact of the chronic effects of seizures over time on human cortex can not be excluded. This confounding factor is in part why we referenced our findings to the known physiology of amplitude modulation (i.e., mu-beta amplitude reductions/gamma amplitude increases) that has been demonstrated in both invasively monitored subjects and in normal healthy subjects (2, 3, 10). Numerous studies have shown that if a seizure focus is involved in a given region of the brain, this is typically associated with a reduced cognitive performance. This property underpins that seizures are typically disruptive and do not augment cortical function. Thus, the superior performance of FSNs at identifying behavior compared with amplitude modulation is unlikely to be attributed to this pathologic phenomenon.

Third, it is important to note that the previously described measures of synchrony described by Mormann et al., although superbly done, are taken from histologically and developmentally distinct regions of brain (8). Depth electrodes placed in the hippocampus/mesial temporal lobe are recording from the allocortex. The allocortex is a heterogenetic cortex, because during development it never has the six-layered architecture of the homogenetic neocortex (what was evaluated in this study with surface electrodes over lateral frontal/temporal/parietal regions). It also differs from the heterotypic cortex, a type of neocortex that, during prenatal development, passes through a six-layered stage to have less layers (e.g., agranular area 4 of Brodmann) or more layers (e.g., striate area 17 of Brodmann) in the mature brain. Thus, one has to be somewhat cautious about fully attributing these synchrony findings to other regions of the brain whose cytoarchitecture is fundamentally different.

Fourth, our analytic methodology would likely accommodate epilepsy-related alterations in cortical physiology that were not directly task relevant. Specifically, with the PCA signal decomposition and DFA, the aggregated SPs of either epilepsy-induced continuous uniform synchronous signals, or random episodic synchronous events, would be separated from the task-specific patterns that occur consistently during temporally constrained epochs in time.

FSN Analysis of Simulated EEG Data. The FSN methods used by this work were applied to invasive electrophysiologic data. To explore the applicability of these methods to more widely used noninvasive EEG, we created a simulated noninvasive signal from the ECoG signal. EEG signal has two main differences from ECoG in terms of signal resolution that may affect applicability of the FSN methods. First, there is a difference in anatomic spatial resolution of the measured electrophysiology as a result of greater separation of the sensors (electrodes) from the measured cortical activity (i.e., above the scalp vs. on the cortical surface). Second, there is a reduced sensitivity to physiologically relevant signals in the frequency domain above 30–40 Hz (11). In this section, we test the effects of these limitations of EEG on the results of the FSN methods. To be clear, the results discussed here are obtained from simulated EEG data and not real EEG data. Although this allows us to test the effects of the previously mentioned limitations on the FSN methods without introducing the confounds that arise when different data sets are used, such as difference in cognitive task performance and mental state, it does not account for the effects of the increased anatomic coverage of EEG relative to ECoG.

Simulating EEG data. To simulate the limitations of EEG signal in the ECoG data sets used in this work, both spatial and frequency filtering were applied to the raw ECoG signal before processing. No other changes were made to the signal, metadata (i.e., trial labels and VOT times), or analysis parameters. The frequency filter applied was a simple low-pass filter with a cutoff at 30 Hz, which provided for a conservative simulation of the limitations of EEG in the frequency domain.

The spatial filter applied is depicted in the Fig. S8 *A*–*C*. Each simulated EEG channel was computed as the weighted sum over a subset of 16 ECoG electrodes. The area of the ECoG grids that contributed to a single simulated EEG electrode is depicted in Fig. S8*A*. The relative weights in the sum of the 16 electrodes that contribute to a single simulated EEG electrode are shown in Fig. S8*B*. The spatial filter was used to down sample the 64- and 48-electrode ECoG grids to nine and six EEG channels, respectively. A full simulated nine-channel EEG grid is illustrated in Fig. S8*C*. Simulated EEG grids from 48-channel ECoG grids only included the top six rows of ECoG electrodes in Fig. S8*A* and top two rows of Fig. S8*C*.

Effects of EEG spatial and spectral limitations on the FSN analysis methods. The EEG simulation described previously produced two notable results. First, similar to ECoG, simulated EEG FSNs outperformed the simulated EEG ARs for the rest vs. speech cognitive task. Second, unlike ECoG, neither the simulated EEG ARs nor FSNs discriminated phonemes at an above-chance level.

These results are further detailed in Fig. S8 *D* and *E*. Similar to Fig. 3*A*, Fig. S9*D* shows the temporal periods for which significant ARs and FSNs from the simulated EEG data significantly distinguish rest from speech. The blue and black boxes mark temporal periods (from 1 to 37, left to right) that had significant ARs and FSNs, respectively, for subjects 1–5. There were more significant FSNs than ARs for each of the five subjects. Compared with Fig. 3*B*, the significantly distinguished periods for the simulated EEG (both AR and FSNs) are less than that found for ECoG data in all cases.

This point is further highlighted by Fig. S7*E*, which shows the distributions over subjects of the number of significant ARs and FSNs found for the rest vs. speech cognitive task (left two columns) and all phoneme discriminant cognitive tasks (right two columns). The horizontal lines with stars indicate that significantly more (paired t test, $P < 0.05$) simulated EEG FSNs that discriminate rest and speech were found than any other condition. The figure also indicates that the number of significant phoneme discriminant ARs and FSNs found in simulated EEG data were not significantly different and, in fact, were generally at the level of expected false discoveries for the phoneme discrimination task (indicated by the vertical dotted line). This result is unsurprising given the important role that gamma rhythms (which are not accessible with EEG) play in parsing information content of phonemic articulation (12).

In conclusion, the FSN methods do show an advantage over ARs even when the frequency and spectral resolution limitations of EEG are applied in distinguishing task vs. rest. It does not, however, overcome some of the fundamental limitations of EEG in distinguishing subtasks (i.e., phonemes) that are possible with more anatomically and spectrally resolved invasive signals.

1. Benjamini Y, Hochberg Y (1995) Controlling the false discovery rate: A practical and powerful approach to multiple testing. *J Roy Stat Soc B Met* 57(1):289–300.
2. Crone NE, Miglioretti DL, Gordon B, Lesser RP (1998) Functional mapping of human sensorimotor cortex with electrocorticographic spectral analysis. II. Event-related synchronization in the gamma band. *Brain* 121(Pt 12):2301–2315.
3. Crone NE, et al. (1998) Functional mapping of human sensorimotor cortex with electrocorticographic spectral analysis. I. Alpha and beta event-related desynchronization. *Brain* 121(Pt 12):2271–2299.
4. Gaona CM, et al. (2011) Nonuniform high-gamma (60-500 Hz) power changes dissociate cognitive task and anatomy in human cortex. *J Neurosci* 31(6):2091–2100.
5. Pohar M, Blas M, Turk S (2004) Comparison of logistic regression and linear discriminant analysis: A simulation study. *Metodolski Zvezki* 1(1):143–161.
6. Maris E, Oostenveld R (2007) Nonparametric statistical testing of EEG- and MEG-data. *J Neurosci Methods* 164(1):177–190.
7. Frey BJ, Dueck D (2007) Clustering by passing messages between data points. *Science* 315(5814):972–976.
8. Mormann F, et al. (2003) Epileptic seizures are preceded by a decrease in synchronization. *Epilepsy Res* 53(3):173–185.
9. Amor F, et al. (2009) Cortical local and long-range synchronization interplay in human absence seizure initiation. *Neuroimage* 45(3):950–962.
10. Pfurtscheller G, Berghold A (1989) Patterns of cortical activation during planning of voluntary movement. *Electroencephalogr Clin Neurophysiol* 72(3):250–258.
11. Nunez PL, Srinivasan R (2006) *Electric Fields of the Brain: The Neurophysics of EEG* (Oxford Univ Press, New York), 2nd Ed, p xvi.
12. Leuthardt EC, et al. (2011) Using the electrocorticographic speech network to control a brain-computer interface in humans. *J Neural Eng* 8(3):036004.

A

	b_t	c_n	h_d	l_d	m_n	p_p	r_d	s_t	t_n
[ɛ]	bet	ken	head	led	men	pep	red	set	ten
[æ]	bat	can	had	lad	man	pap	rad	sat	tan
[i]	beat	keen	heed	lead	mean	peep	read	seat	teen
[u]	boot	coon	hood	lewd	moon	poop	rood	soot	toon

B

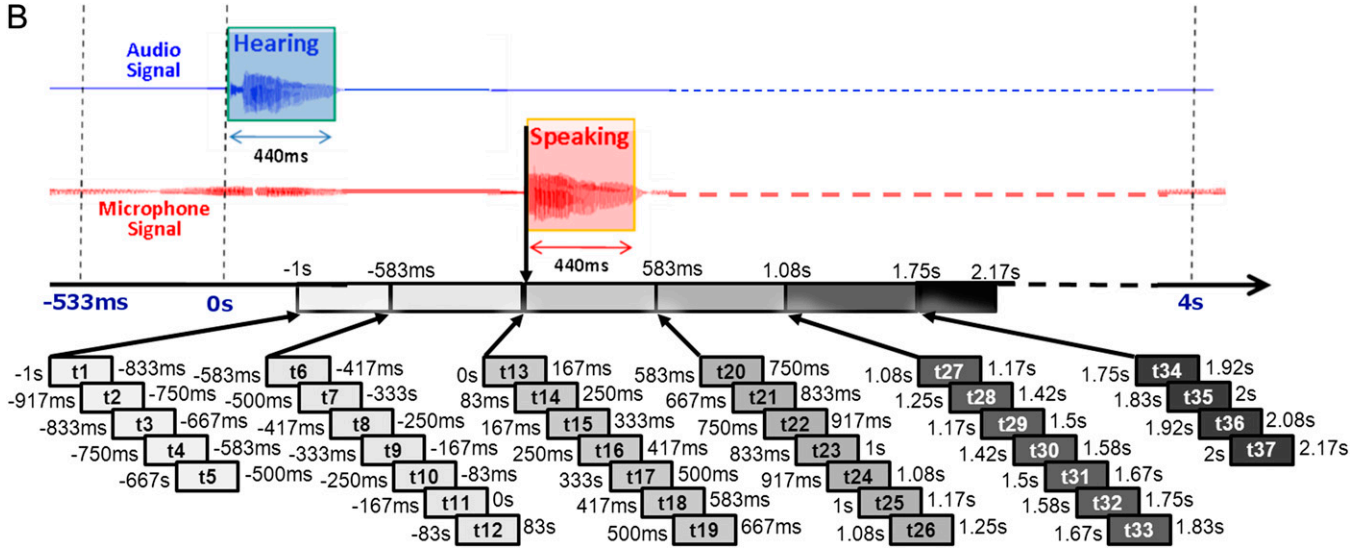

Fig. S1. (*A*) Table of task words. (*B*) Task timing. The relative timing of the audio cues and recorded spoken responses are depicted with the blue and red lines, respectively. Time is represented on the *x* axis. The 37 analyzed time periods relative to voice onset time (VOT) are listed in the gray boxes at the bottom of the figure with arrows indicating the relative positions in time. The three vertical dashed lines indicate 533 ms before audio cue, audio cue time, and 4 s after audio cue, respectively, from left to right.

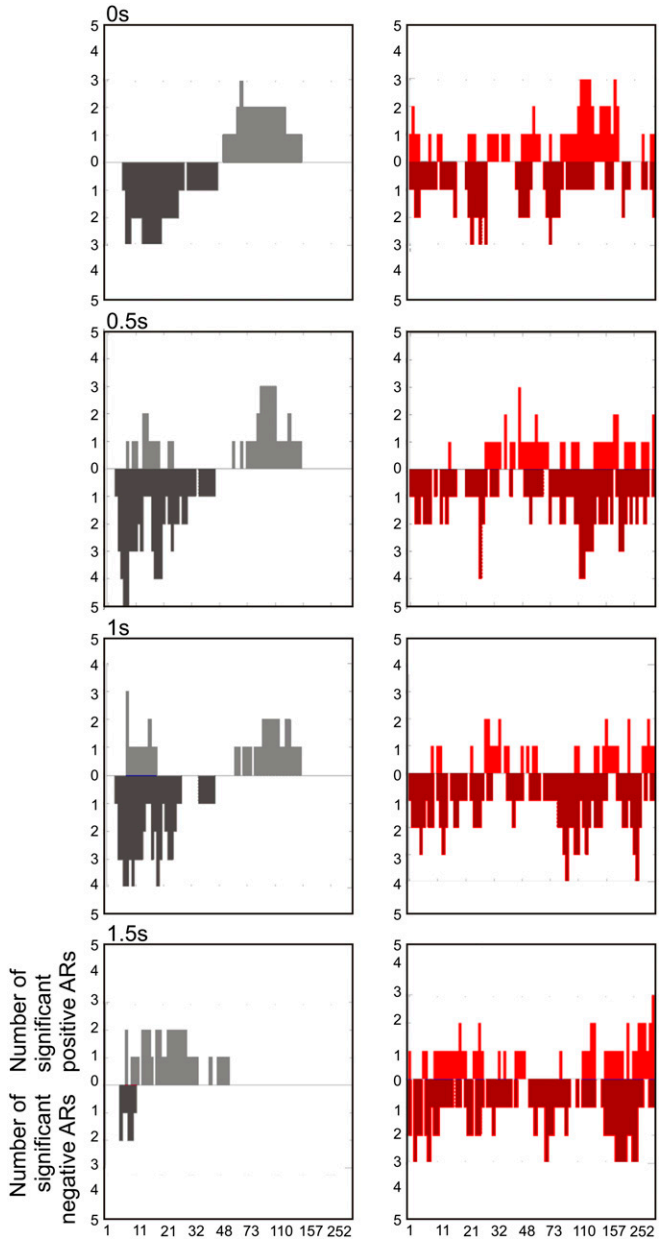

Fig. S2. ARs- and FSNs-based pseudospectra over time. The time periods, including the 0-, 0.5-, 1-, and 1.5-s time samples relative to voice onset time (i.e., t12, t18, t24, and t30) are in the rows from top to bottom. The left column shows the number of ARs (*y* axis) with significant increases and decreases in gray and dark gray, respectively, for each spectral bin (*x* axis). The right column gives the number of FSNs with significant increases and decreases in red and dark red, respectively. Significant ARs were those with $P < 0.05$. Significant frequency bins within the FSNs were taken as the bins for which the SE across the spectral patterns for all of the electrodes in the same FSN spectral grouping was above or below zero.

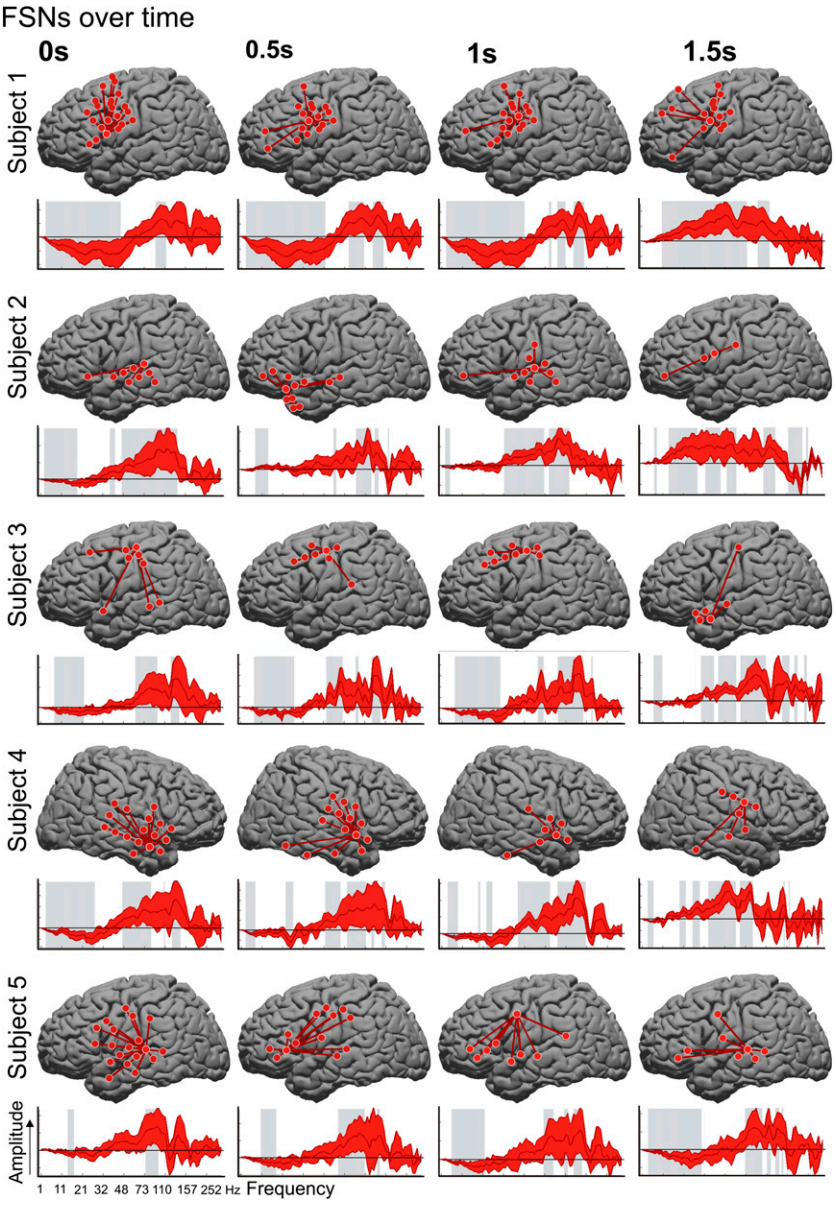

Fig. S3. Changing topographies and their spectral characteristics at VOT, and 0.5, 1, and 1.5s after VOT (in columns from left to right for subjects) for subjects 1–5 (in rows from top to bottom). Anatomic location electrodes included in each FSN are depicted as red circles on the top brain plots. The mean and SEs of the spectral patterns are shown, respectively, with the dark red line and shaded red areas in the bottom spectral plots across the electrodes included in each FSN. The shaded gray areas indicate spectral bands with SEs that are either above or below zero.

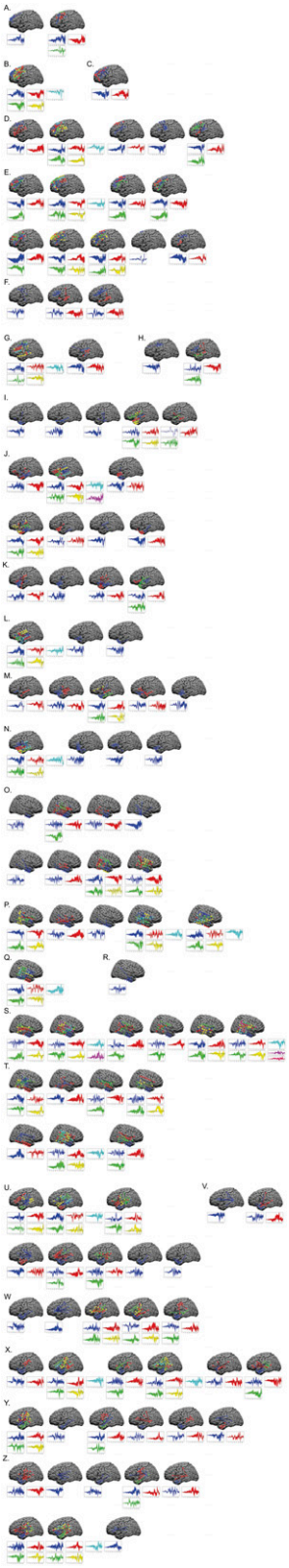

Fig. S4. Significant phoneme discriminant FSNs for all subjects: subject 1 (*A–E*), subject 2 (*F–H*), subject 3 (*I–N*), subject 4 (*O–T*), and subject 5 (*U–Z*). (*A*) Significant [i] vs. [æ] discriminant FSNs at time points t12 and t15. (*B*) Significant [i] vs. [u] discriminant FSN at time point t12. (*C*) Significant [ɛ] vs. [æ] discriminant FSN at time point t9. (*D*) Significant [ɛ] vs. [u] discriminant FSNs at time points t6, t7, t16, t22, and t37. (*E*) Significant [æ] vs. [u] discriminant FSNs at time points t4, t5, t6, t7, t8, t23, t24, t29, and t34. (*F*) Significant [i] vs. [æ] discriminant FSNs for subject 2 at time points t4, t35, and t36. (*G*) Significant [i] vs. [ɛ] discriminant FSNs for subject 2 at time points t9 and t18. (*H*) Significant [ɛ] vs. [u] discriminant FSNs for subject 2 at time points t10 and t23. (*I*) Significant [i] vs. [æ] discriminant FSNs at time points t4, t15, t22, t30, and t31. (*J*) Significant [i] vs. [ɛ] discriminant FSNs at time points t15, t19, t20, t21, t22, t24, and t25. (*K*)

Legend continued on following page

Significant [i] vs. [u] discriminant FSNs at time points t1, t2, t30, and t33. (*L*) Significant [ɛ] vs. [æ] discriminant FSNs at time points t15, t20, and t24. (*M*) Significant [ɛ] vs. [u] discriminant FSNs at time points t2, t14, t19, t24, and t33. (*N*) Significant [æ] vs. [u] discriminant FSNs at time points t13, t14, t15, and t20. (*O*) Significant [i] vs. [æ] discriminant FSNs at time points t3, t7, t8, t9, t14, t23, t26, and t30. (*P*) Significant [i] vs. [ɛ] discriminant FSNs at time points t8, t9, t14, t19, and t27. (*Q*) Significant [i] vs. [u] discriminant FSNs at time point t2. (*R*) Significant [ɛ] vs. [æ] discriminant FSNs at time point t14. (*S*) Significant [ɛ] vs. [u] discriminant FSNs at time points t8, t16, t19, t20, t22, and t23. (*T*) Significant [æ] vs. [u] discriminant FSNs at time points t7, t8, t11, t13, t14, t15, and t16. (*U*) Significant [i] vs. [æ] discriminant FSNs at time points t7, t15, t16, t22, t26, t27, t28, and t29. (*V*) Significant [ɛ] vs. [u] discriminant FSNs at time points t6 and t10. (*W*) Significant [i] vs. [ɛ] discriminant FSNs at time points t8, t14, t26, and t32. (*X*) Significant [i] vs. [u] discriminant FSNs at time points t19, t20, t34, t33, t35, and t36. (*Y*) Significant [ɛ] vs. [æ] discriminant FSNs at time points t1, t2, t6, t11, t16, and t18. (*Z*) Significant [æ] vs. [u] discriminant FSNs at time points t15, t16, t17, t19, t21, t22, t23, and t34.

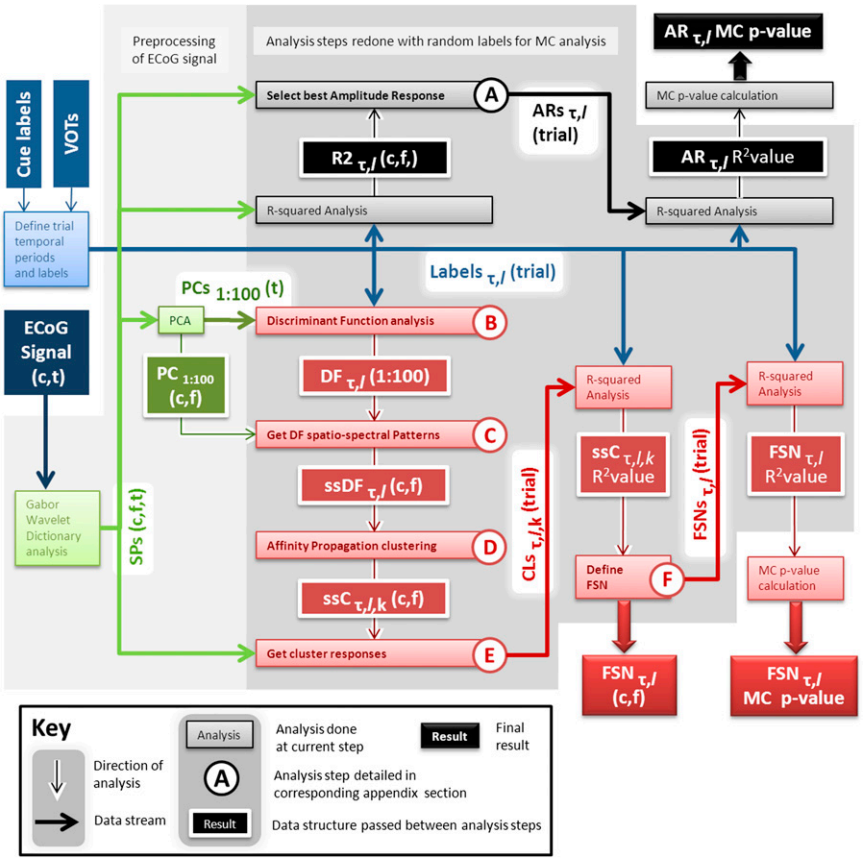

Fig. S5. Diagram of analysis pipeline described in *SI Text*.

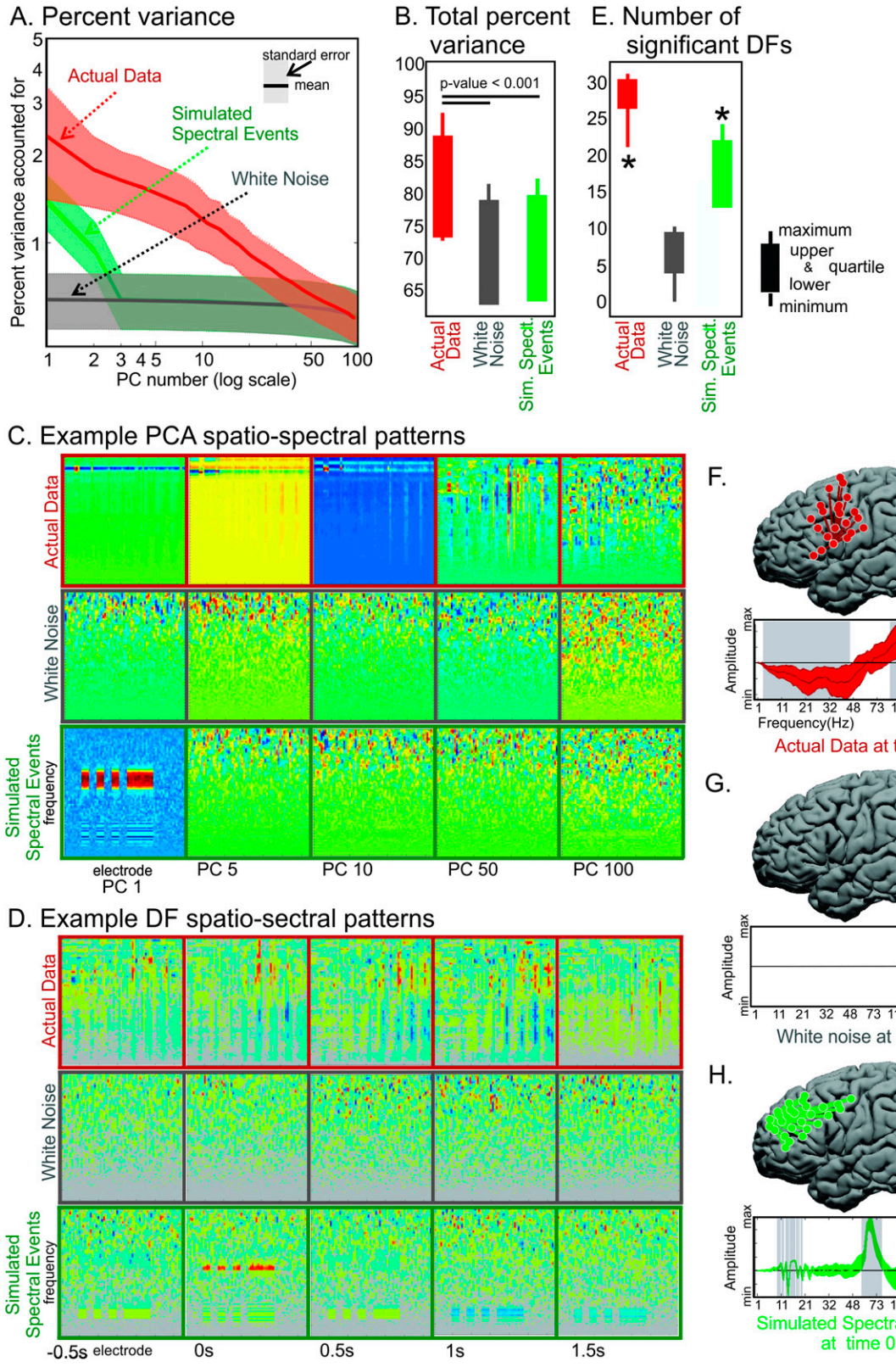

Fig. S6. Results of analysis run on white noise and simulated spectra events data. (*A*) Plot of percent variance in data accounted for on the *y* axis over the first 100 principal components (PCs) on the *x* axis. The red, gray, and green lines plot the mean percent variance across the five subjects for the real data (ECoG signal reported in the paper), white noise signals, and simulated spectral events over the first 100 PCs, respectively. The shaded light red, light gray, and light green areas represent the limits of the SE for real data, white noise, and simulated spectral events across the five subjects over the first 100 PCs, respectively. (*B*) Distributions of percent variance accounted for in total for the first 100 PCs for the real data (red box and whiskers), white noise (gray box and whiskers), and simulated spectral events (green box and whiskers) over the five subjects. The black lines indicate that the distribution of the real data were significantly higher

Legend continued on following page

than that of the white noise and simulated spectral events (pairwise *t* test, $P < 0.001$). (*C*) Example PCs 1, 5, 10, 50, and 100 (respective columns from left to right) for real data (top red highlighted row), white noise (middle gray highlighted row), and simulated spectral events (bottom green highlighted row) from subject 1. The plot represents increases (red) and decreases (blue) in amplitude over electrode number (*x* axis) and frequency (*y* axis). (*D*) Example discriminant function (DF) patterns for the time periods centered at 0, 0.5, 1, 1.5, and 2 s after VOT (respective columns from left to right) for real data (top red highlighted row), white noise (middle gray highlighted row), and simulated spectral events (bottom green highlighted row) from subject 1. Again, the plot represents increases (red) and decreases (blue) in amplitude over electrode number (*x* axis) and frequency (*y* axis). (*E*) Distributions of number of significant DFs (null hypothesis rejected time periods) for the real data (red box and whiskers), white noise data (gray box and whiskers), and simulated spectral events (green box and whiskers). Each data type for which the number of significant hypothesis was significantly greater (using a pairwise *t* test over subjects) than the number of expected false discoveries is indicated with an asterisk. (*F*) Example FSN found in the real data from subject 1 at the time period centered at VOT. (*G*) Example FSN found in the white noise data from subject 1 at the time period centered at VOT. (*H*) Example FSN found in the simulated spectral events data from subject 1 at the time period centered at VOT.

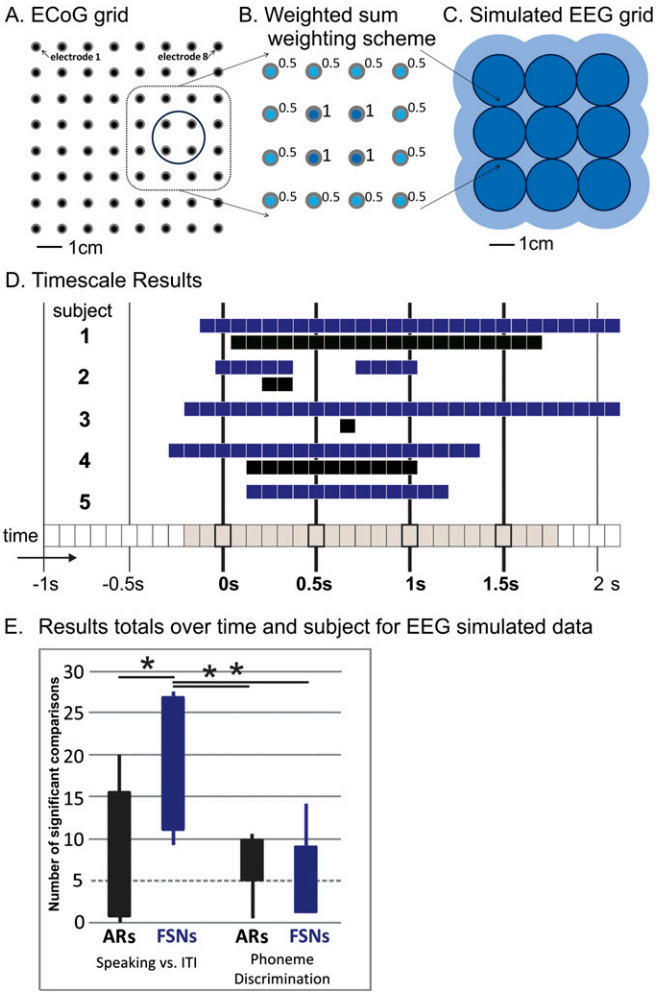

Fig. S7. Methods and results for analysis run on simulated EEG data. (*A*) Representative ECoG grid configuration. (*B*) Spatial weighting schemed used in the weighted sum used in the simulated EEG data spatial filter. (*C*) Scaled simulated EEG grid configuration. (*D*) Significant speaking vs. rest time periods for subjects 1–5 (top to bottom rows). Time points with a significant AR and/or FSN in the simulated EEG data are indicated by black and blue rectangles, respectively. The vertical black lines indicate the time periods that include the –1-, –0.5-, 0-, 0.5-, 1-, 1.5-, and 2-s time samples relative to voice onset time. (*E*) Distributions of the number of significant time periods for ARs (black) and FSNs (blue) in simulated EEG data summed over subjects for the rest vs. speech (leftmost two boxes) and all phoneme discriminant conditions (rightmost two boxes).

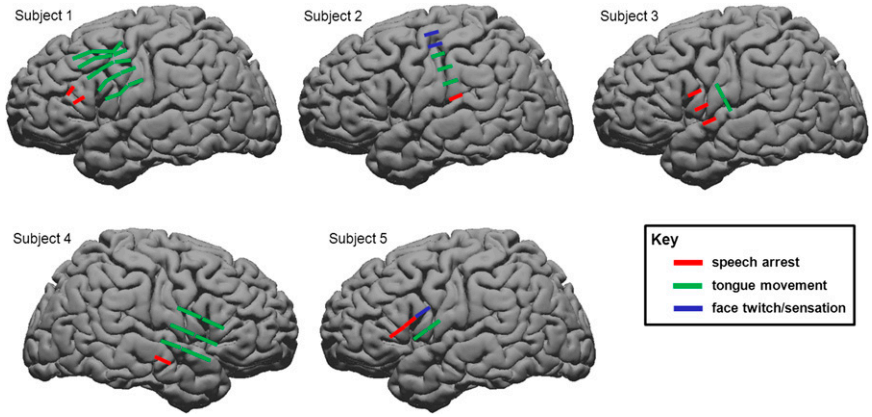

Fig. S8. Cortical stimulation mapping results for subjects 1–5. The bold line plotted on the brains represents the bipolar stimulation positive sites for speech arrest (red), induced tongue movement (green), and induced facial twitches or sensation (blue). The lines connect the locations of the pair of electrodes across which the stimulation was given.

Table S1. Patient demographics

Subject	Age	Sex	IQ	Age of seizure onset	Seizure focus	Handedness	Anti-epileptic medications	ECoG implant description
1	58	F	116	10 y	SFG	Right	KP, CBZ	8 × 8 grid over the left FC
2	48	F	86	1.5 y	MTL	Left	CLP, DPH, PG, OXC	8 × 8 grid over the left FPC
3	49	F	100	10 mo	ATL	Right	KP, TP	4 × 8 grid over the left TC
4	46	F	81	~26 y	ITL	Ambidextrous	LTG, LA, TP, ZNA	4 × 8 grid over the right FPTC
5	36	M	71	1 y	ATL	Left	DK, TP	4 × 8 grid over the left FPTC

ATL, anterior temporal lobe; CBZ, carbamazepine; CLP, clonazepam; DK, depakote; DPH, phenytoin; DZ, diazepam; FC, frontal cortex; FPC, frontal-parietal cortex; FPTC, frontal-parietal-temporal cortex; ITL, inferior temporal lobe; KP, levetiracetam; LA, lorazepam; LTG, lamotrigine; MTL, mesial temporal lobe; OXC, Oxcarbazepine; PG, pregabalin; SFG, superior frontal gyrus; TC, temporal cortex; TP, topiramate; ZNA, zonisamide.

Table S2. Data composition

Subject	Recording electrodes	Number of task runs	Number of audio cued words	Number of valid spoken responses	Number of valid [i] trials	Number of valid [ɛ] trials	Number of valid [æ] trials	Number of valid [u] trials
1	64	6	216	213	53	52	54	54
2	64	6	216	216	54	54	54	54
3	48	6	216	214	54	52	54	54
4	48	5	180	177	44	43	45	45
5	48	4	144	143	36	36	35	36